

Biomolecular condensates mediate C–N bond formation

Received: 22 July 2025

Accepted: 10 February 2026

Published online: 25 March 2026

 Check for updates

Xiaowei Song¹, Yuefeng Ma², Michael W. Chen², Wen Yu^{2,3}, Xiao Yan⁴,
Jinheng Xu¹, Lecheng Lyu¹, Anthony A. Hyman⁴, Yifan Dai^{2,3}✉ &
Richard N. Zare¹✉

We discover that biomolecular condensates, formed by intrinsically disordered proteins without inherent chemical activity, can spontaneously drive nonenzymatic reductive amination. These condensates facilitate reactions between amines and aldehydes or ketones, yielding imines, which are subsequently hydrogenated to form alkylated amines leading to C–N bond formation. Our experiments show that condensates modulate the reductive amination of diverse types of metabolite containing carbonyl groups. Using combinatorial metabolomics, we found that condensates generate previously unknown metabolites through the dimerization of natural amines with ketones and aldehydes. Metabolomics in living cells confirms that the ability of condensates in mediating C–N bond formation enables the synthesis of new metabolites and regulates cellular pathways. These findings uncover a previously unrecognized inherent function of biomolecular condensates, redefining their roles in metabolism. This further highlights the broader influence of condensates on chemical homeostasis and biochemical regulation in biological and prebiotic chemistry.

Phase transitions of biomacromolecules^{1,2}, which lead to the formation of biomolecular condensates^{3–6}, have transformed our understanding of how living systems regulate diverse cellular processes in a spatiotemporal manner. Current understanding of the functions of biomolecular condensates primarily stems from the sequestration and enrichment effects generated by phase separation^{4–8}. However, such understanding does not fully justify the necessity of a new phase, as the same functional effects can similarly be achieved through the formation of stoichiometric complexes^{9–11} and the creation and maintenance of a distinct new phase is thermodynamically costly^{3,12–14}.

Recent research has shown that phase separation, albeit driven by the phase transition of intrinsically disordered proteins (IDPs), is a density transition of the whole solution system^{15–20}. The asymmetric nature of this transition process, which can be driven by various factors, including hydrophobicity, charge fraction, interaction pairs and chain

flexibility^{19,21–23}, mediates the density gradients of biomacromolecules, ions and water molecules between condensates and the coexisting phases, which collectively define a Galvanic electric potential^{17,20,23,24}. This electric potential gradient manifests as an interfacial electric potential at the surface of the condensate, generating an interfacial electric field^{15,17,25}. Similarly, because of the existence of large surfaces of condensates in the solution²⁶, these surfaces exert forces in the solvent environment and break the homogeneous nature of solvent molecules, creating a liquid–liquid interface with aligned dipole moments (for example, by oriented water molecules), which encodes their noncentrosymmetric property^{20,27}. Such noncentrosymmetric surfaces, no matter their own surface electrostatic charges, can generate a surface dipole field^{20,28}, which is also part of the contribution to the interfacial electric field^{17,29}. These properties can alter bond ionicity and modulate local water activity^{17,29,30}, which changes the reaction free energy of the

¹Department of Chemistry, Stanford University, Stanford, CA, USA. ²Department of Biomedical Engineering, Washington University in St. Louis, Saint Louis, MO, USA. ³Center for Biomolecular Condensates, Washington University in St. Louis, Saint Louis, MO, USA. ⁴Max Planck Institute of Molecular Cell Biology and Genetics, Dresden, Germany. ✉e-mail: dyifan@wustl.edu; rnz@stanford.edu

chemicals^{30–32}, providing the electrochemical and chemical environmental basis for the observed spontaneous redox activities and the inherent catalytic behaviors of condensates^{15,17,29,33–36}. These recent discoveries suggest that condensates are electrochemically active and may have broad, nonspecific biochemical functions, operating at scales larger than the molecular level^{31,37,38}. These inherent functions of condensates, which are distinct from the molecular functions encoded in the specific constituents of condensates, highlight the importance of establishing a second liquid phase for cellular biochemistry. However, the breadth of the biochemical functions of condensates remains largely unexplored.

A fundamental chemistry essential for cellular biochemical functions is the formation of C–N bonds^{39,40}. C–N bond formation is critical for synthesizing key biomolecules, including amino acids, nucleotides and nitrogen-containing saccharides, which participate in processes such as the urea cycle, amino acid metabolism, cellular signaling and nucleotide biosynthesis⁴¹. This process is typically driven by enzymes^{39,40}, including imine reductases, transaminases, nitrogenase and S-adenosylmethionine-dependent methyltransferases. The underlying functioning mechanism of these enzymes depends on the capability of the catalytic center to align the dipole moments of the reactants, thereby lowering their activation free energy through the internal electric field within the catalytic center and facilitating electrophilic attack between the reactants^{42–45}. These features are consistent with the fundamental electrochemical properties of condensates^{15,17,26,29}, which are also similar to diverse electrochemically active liquid–air, liquid–liquid and liquid–solid interfaces^{30,46–52}. As such, we wondered whether biomolecular condensates may promote nonenzymatic C–N bond formation on a global scale.

In this study, we demonstrate that biomolecular condensates facilitate spontaneous C–N bond formation through nonenzymatic reductive amination. Through *in vitro* reconstitutions of condensate-based reactions and metabolomics in living cells, we show that condensates can mediate the reductive amination and alkylated modification reactions between 18 amines and 10 carbonyl metabolites, producing previously unreported metabolites with structural diversity through cross-reactions. Metabolomic analyses in living cells further suggest that condensates facilitate novel metabolic pathways and may regulate cellular reactions. Our discovery suggests that the distinct physical scale of condensates, compared to their molecular constituents, gives rise to emergent functions. The capability of condensates to mediate nonenzymatic chemistry underscores their essential roles in maintaining chemical homeostasis and metabolic regulation in cells.

Results

Biomolecular condensates enable C–N bond formation

To explore the potential chemical activities of condensates, we first used a model biomolecular condensate formed by the wild-type resilin-like polypeptide (RLP)^{53,54}. RLP shares similar sequence features with many phase-separating IDPs, such as FUS and DDX4 (refs. 55–58) and can drive an asymmetric phase transition, setting up an interphase electric potential and a strong interfacial field^{15,20,29}. The RLP condensate can drive spontaneous redox reactions (for example, production of reactive oxygen species¹⁵) and catalyze hydrolysis reactions (for example, decomposition of ATP²⁹) on the basis of its interfacial field and internal chemical environments. Thus, these electrochemical properties make the RLP condensate an excellent system for studying the inherent nonenzymatic biochemical functions of condensates.

We hypothesized that the unique condensate solvent environment, the polarity difference between the phases and the interfacial electric field on condensate surface could favorably contribute to the solvation and enrichment of substrates and align their dipoles^{15,19,25,29,59,60}, promoting the nucleophilic attack by amines on carbonyl compounds to form imine. Additionally, the redox activity at the interfacial field could facilitate the reduction of unstable imines

to alkylated amines^{15,61}. This process can potentially lead to C–N bond formation by condensates (Fig. 1a).

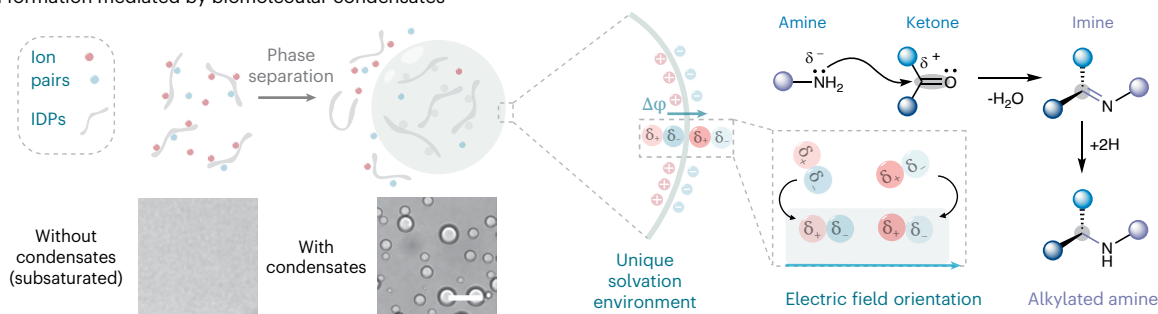
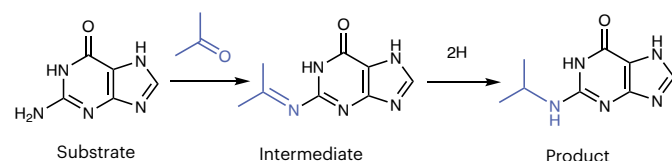
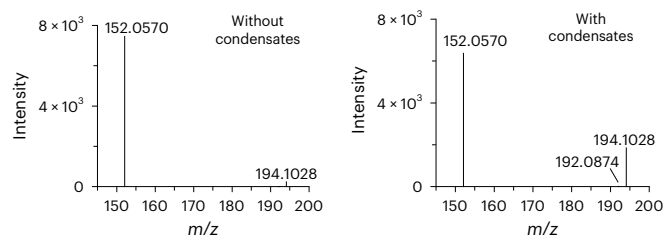
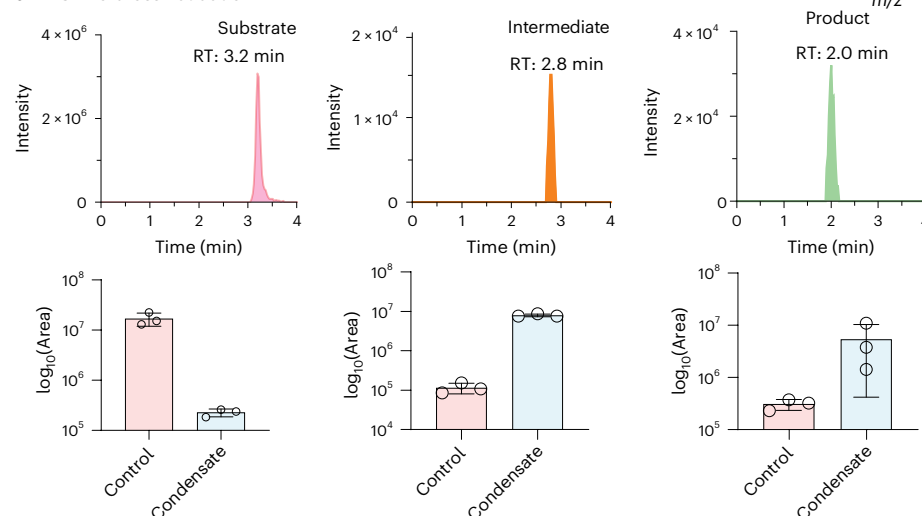
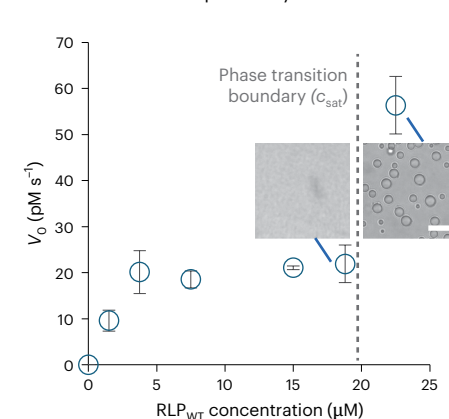
We first implemented a common substrate pair, guanine and acetone (Fig. 1b), which respectively provide an amine group and a carbonyl group, to assess the ability of condensates to link them together through C–N bond formation by using nano electrospray ionization mass spectrometry (nESI-MS) and liquid chromatography (LC)–MS. We used a solution without condensates (containing RLP below its saturated concentration c_{sat}) as the control group (without condensates) and a solution with condensates (containing RLP above its c_{sat}) as the test group (with condensates). Compared to the control group, after 3 h of incubation at room temperature, in the condensate group, we identified a tenfold increase in the product, *N*-isopropylguanine (Fig. 1c). We further analyzed the same reaction using LC–MS to exclude the possibility of in-source reaction caused by microdroplets in the nESI-MS. We found a clear separation in retention times among the substrate, imine intermediate and the *N*-isopropyl product. In the condensate group, we observed a substantial decrease in the substrate and significant increases for the intermediate and the product (Fig. 1d). Lastly, to confirm that this reaction capability is condensate dependent, we evaluated the initial reaction rate in an RLP concentration-dependent manner (Fig. 1e). We found that the reaction rate rose exponentially once the RLP concentration surpassed its c_{sat} , confirming that this reaction is phase separation dependent²⁹. These results collectively confirm the capability of the condensate solution on mediating C–N bond formation.

Interfacial effect of condensates on driving C–N reactions

To enable the study of C–N bond formation at an individual condensate level, we designed a fluorogenic assay (Fig. 2a), in which the formation of C–N bond can alter the fluorescence emission of the reactants. Specifically, by scanning the shift of fluorescence emission with an excitation laser set at 405 nm, we identified that the C–N formation reaction between *N,N*-dimethyl-6-propionyl-2-naphthylamine and 4-amino-1,8-naphthalimide can lead to a substantial decrease in emission at ~450 nm while causing an increase in emission at ~560 nm (Fig. 2b), allowing us to directly track the reaction of individual condensates through confocal microscopy.

We first verified the C–N bond formation between the two substrates in the condensate group using high-resolution MS (HR-MS) (Fig. 2c). Using confocal microscopy, by comparing the fluorescence distribution profiles of the substrate and the product between the dilute and the dense phases, we found a noticeable decrease in fluorescence signal of the substrate at the interface of the condensate (Fig. 2d). This observation provides direct evidence that the electrochemical environment of condensate interface can potentially contribute to this reaction.

To further analyze the role of interface on modulating this reaction, we set out to perturb the interfacial electrochemical environment of the RLP condensates using a recently demonstrated surfactant-based approach²⁰. We added sodium dodecyl sulfate (SDS) and cetyltrimethylammonium bromide (CTAB), which are surfactants with opposite terminal charges, into the condensate solution, thereby altering the interfacial electrochemical environments of the condensate²⁰. We verified that the zeta potentials of condensates with and without SDS or CTAB are different (Supplementary Fig. 1a). Specifically, condensates modified with SDS showed the most negative zeta potential, suggesting that the highest surface charge density⁶², which corresponds to the strongest interfacial electric field³⁰. Then, using the ratiometric signal between the product and the substrate obtained from the fluorescence reaction assay, we compared the reaction capability of different types of condensates with similar size (Supplementary Fig. 1b). We found that aligning with the trends of zeta potential, the condensates with SDS showed the strongest ability on driving the C–N bond formation under the same reaction conditions. These observations suggest that

a C–N bond formation mediated by biomolecular condensates**b** Reductive amination of guanine and acetone by condensates**c** nESI-MS**d** LC-MS cross-validation**e** Concentration dependency**Fig. 1 | Biomolecular condensate spontaneously drives C–N bond formation.**

a, Schematic representation of condensate-mediated C–N bond formation. Phase separation of IDPs defines a solvent gradient between phases, which generates a unique solvation environment in the dense phase and an interphase electric potential gradient. The solvation environment can alter the properties of the substrates. The interphase electric potential gradient sets up an interfacial electric double layer, serving as an electric field to mediate polarity-dependent reductive amination reaction. Inset: graph showing the confocal differential interference contrast images of control solution ($c_{\text{IDP}} < c_{\text{sat}}$) and condensate solution ($c_{\text{IDP}} > c_{\text{sat}}$). Scale bar, 5 μm . **b**, Reductive amination of guanine and

acetone forms an intermediate imine and a final product *N*-isopropylguanine. **c**, nESI-MS analysis of the reaction using solution with or without condensates. **d**, LC-MS analysis of the reaction using solution with or without condensates. Data points represent the mean \pm s.d. ($n = 3$ replicates). Statistical analysis was performed using a two-tailed *F*-test: $P = 0.0001$ (substrate), 0.0066 (intermediate) and 0.0004 (product). RT, retention time. **e**, IDP concentration-dependent initial rate of the reaction shows that this reaction is phase separation dependent. Inset: figures showing the solutions containing the reactants and different concentrations of RLPs. Scale bar, 5 μm . Data points represent the mean \pm s.d. ($n = 3$ replicates).

interfacial electrochemical environments can be a key contributor to the chemical function of condensates ('Discussion').

Reductive amination of aldehydes, ketones and ketoacids

We next expanded the chemical reaction landscape and assessed the reductive amination of native ketoacids with ammonium ions by condensates. When ammonium hydroxide is added into water, it completely dissolves to produce NH_4^+ ions. NH_4^+ in the presence of water acts as a weak acid and it is in equilibrium with NH_3 and H_3O^+ with a K_a of about 5.6×10^{-10} at 298 K (ref. 63), generating NH_3 as the reagent for reductive amination. Ketoacids are major precursors for amino acid biosynthesis, typically requiring enzymatic imine reductases to generate stable amines⁶⁴. With the further addition of only ammonium ion

into solutions, we evaluated the relative abundance of each product ion compared to the sum of a substrate ion and a product ion. We surprisingly detected the generation of aspartate (15%), β -aminobutyrate (3%), alanine (4%) and glutamate (3%) from oxaloacetate, acetoacetate, pyruvic acid and α -ketoglutarate, respectively (Fig. 3a). In contrast, no correspondent amino acids were successfully detected in the control groups. The negative detection results were also observed from another additional condensate group with the absence of ammonia, indicating that the RLP is not the ammonia source for the reductive amination (Supplementary Fig. 2).

To confirm the involvement of ammonium ions and rule out false positive results caused by the presence of protein, we used isotope-labeled ammonium chloride ($^{15}\text{NH}_4\text{Cl}$) to perform the

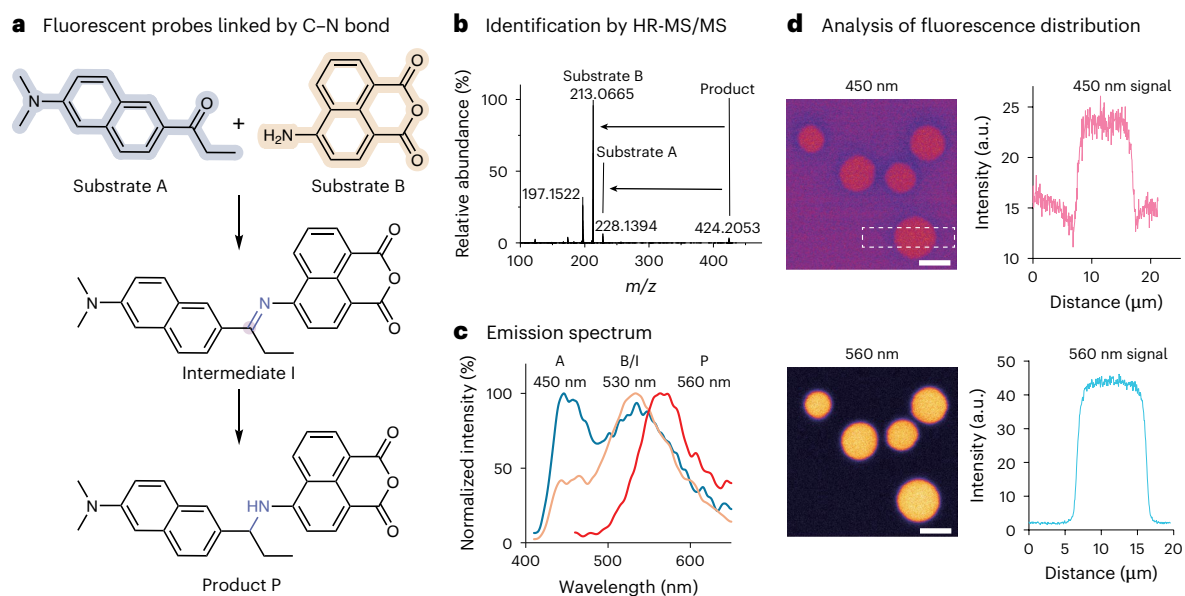


Fig. 2 | Confocal fluorescence microscopy verification of the C–N bond formation by condensates. **a**, Diagram of C–N bond formation between two selected substrates. **b**, HR-MS analysis of fluorogenic reactions using the solution with condensates. **c**, Evaluation of the emission spectrum of fluorogenic

chemicals before and after C–N bond formation. **d**, Confocal fluorescence imaging analysis of condensates with fluorogenic reactions. The fluorescence distribution profiles show that the reactant is depleted at the interface of condensates. A similar result was acquired from $n = 3$ independent experiments.

condensate-mediated reductive amination. We examined the reductive amination reactions using aldehyde and ketone substrates, including acetaldehyde, glyceraldehyde, glyoxylic acid and acetone to react with ammonium ions (Fig. 3b), and found the formation of ethylamine (94% relative abundance), 3-amino-1,2-propanediol (26% relative abundance), glycine (9% relative abundance) and isopropylamine (14% relative abundance) only in solutions containing condensates. The successful detection of the ^{15}N -labeled amino acids in the condensate-containing solution verified the validity of these reactions (Supplementary Fig. 3). These results confirm that condensates can mediate reductive amination of ketones and aldehydes nonenzymatically.

Alkylation of amine-containing metabolites

We next evaluated the ability of condensates in C–N bond formation by expanding the substrate scope to amine metabolites, specifically glucosamine, lysine, sphingosine, cytosine, spermidine and thiamine, to represent the six major categories of amine-containing species, including amino acids, lipids, nucleic acids, polyamines and vitamins⁴¹. These reactants are highly diverse in chemical structures. We introduced formaldehyde, acetaldehyde and acetone into the solution containing condensates and the selected amine metabolites. We found that methylation, ethylation and isopropylation occurred on the amine group of each model metabolite with a substantial increase in relative abundance varied from 1% to 98% compared to the control group (Fig. 3c and Supplementary Figs. 4–6). These results confirm that condensates can afford C–N bond formation using diverse substrates and can tune the structural diversity and complexity of the substrate, similar to naturally occurring *N*-acetylation and *N*-methylation of metabolites⁶⁵. This observation suggests a role of condensates in increasing the chemical complexity, providing the chemical basis for evolving biological functions^{45,66}.

One-pot de novo synthesis of polyamines

With the ability of condensates to mediate C–N bond formation, we next tested whether they could drive one-pot de novo synthesis of polyamines. Polyamines, which are mainly produced from ornithine through decarboxylation, have a critical role in cell proliferation and

differentiation and biomacromolecular synthesis in living cells^{67,68}. They consist of 3–5 carbon units and more than one primary or secondary amine group⁶⁹, linking each other through C–N bonding. Thus, we wondered whether condensates can directly link multiple metabolites based on saturated dialdehydes together to form polyamines. We fed ammonia, malondialdehyde, succinaldehyde and glutaraldehyde as the starting synthons for the one-pot de novo synthesis of four typical polyamines. By feeding the condensate solution with these starting materials at distinct molar ratios shown in Fig. 3d, we observed the production of these four polyamines with a relative abundance around 9% for spermidine, 18% for spermine, 47% for cadaverine and 74% for putrescine (Fig. 3d and Supplementary Figs. 7–10). These results demonstrate an alternative, nonenzymatic route for polyamine synthesis⁶⁸.

Generality of condensate-dependent C–N bond formation

Next, we implemented four distinct native proteins that are known to serve as phase transition drivers, including EWS RNA-binding protein (EWSR), DDX4 low-complexity domain (LCD), fused in sarcoma (FUS) and TATA-binding protein-associated factor 15 (TAF15)^{70,71}. We used established protocols to reconstitute condensates to evaluate their capabilities on driving C–N bond formation using three distinct reactions^{70,71} (Supplementary Fig. 11a). Compared to their subsaturated conditions, the solutions containing condensates showed different abilities to mediate the C–N bond formation (Supplementary Fig. 11b,c). Notably, for the reactions between serotonin and pyruvic acid, all the condensate groups demonstrated substantial enhancement of the production formation (Supplementary Fig. 11d). These observations suggest that the electrochemical properties of condensates are sequence dependent and the solvation properties of distinct chemicals in different types of condensate solvent environment can modulate condensate reaction selectivity ('Discussion').

Combinatorial metabolomics

To explore the scope of condensate-mediated metabolite formation, we conducted a combinatorial metabolomics screen to investigate whether a new metabolite can be generated simply by linking two known ones that carry amine and carbonyl group by condensates (Fig. 4a).

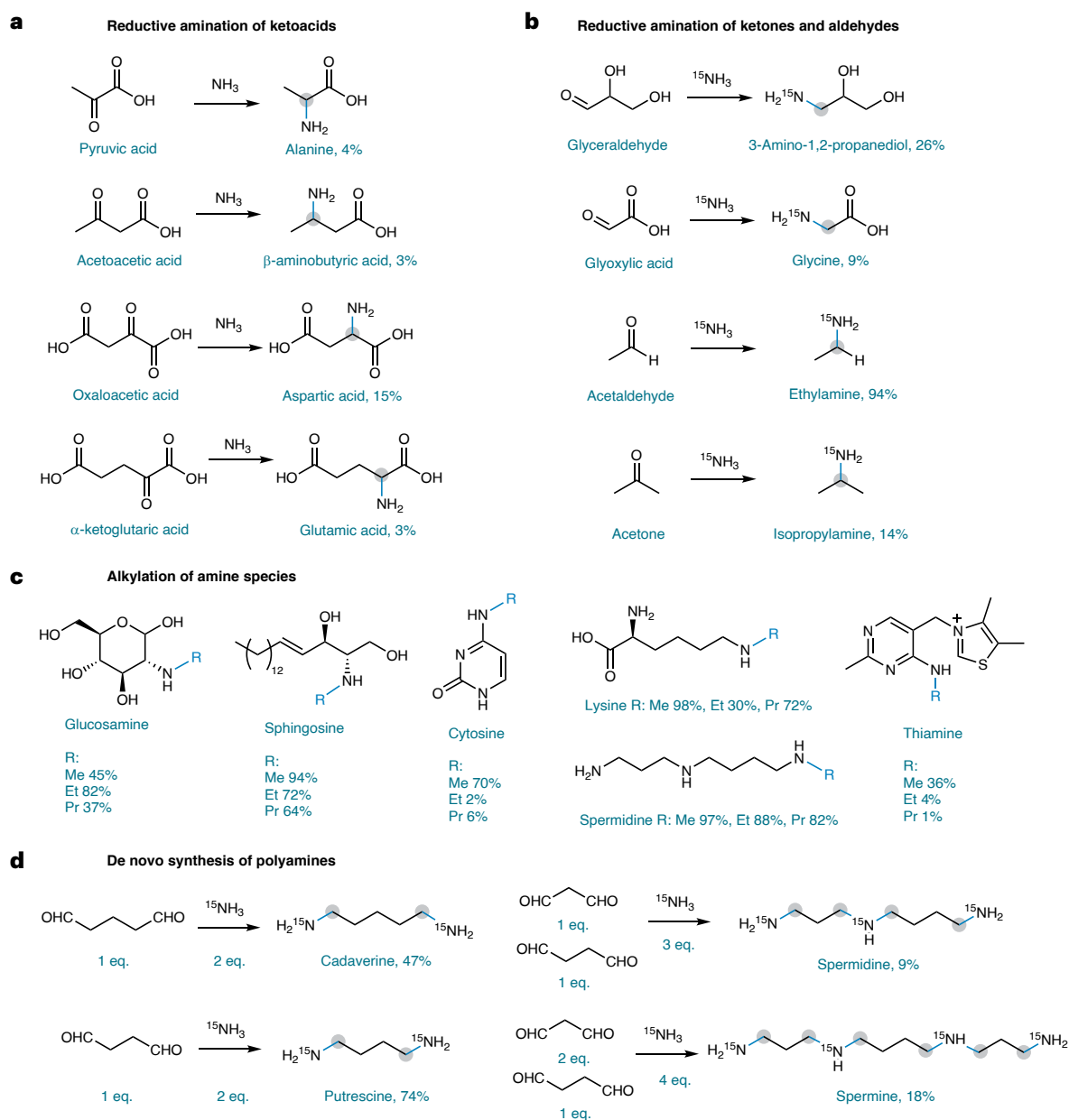


Fig. 3 | Biomolecular condensates enable reductive amination of diverse substrates. a, Reductive amination of ketoacids with ammonium. **b**, Reductive amination of ketone and aldehyde metabolites. Ammonium hydroxide can be incorporated into those carbonyl compounds to form corresponding primary amine metabolites after incubating with condensate solution. $^{15}\text{NH}_4\text{Cl}$ was externally spiked for confirmation. **c**, Alkylation of six major types of amine-containing species in body, which are building blocks of proteins, saccharides,

lipids, nucleic acids, vitamins and polyamines. Alkylation includes methylation (Me), ethylation (Et) and isopropionylation (Pr). **d**, De novo synthesis of polyamines by one-pot strategy driven by condensates. Four typical polyamines (spermine, spermidine, cadaverine and putrescine) can be constructed by C–N bond linking between different amounts of ammonium, glutaraldehyde, succinaldehyde and malondialdehyde at stoichiometric ratio.

Using 18 amines (A_x , where $x = 1\text{--}18$) and 10 carbonyl compounds (K_y , $y = 1\text{--}10$), we found that condensates facilitate C–N bond formation with high abundances ($>60\%$) for carbonyl compounds with a length of 1–3 carbon units (for example, acetone, acetaldehyde, pyruvic acid and glyceraldehyde) and amines with flexible backbones (for example, glycine and sphingosine). It is apparent that the C–N coupling by condensates favors metabolites that have high basicity, high solubility and a flexible carbon backbone, which can achieve a relative abundance higher than 50%. In contrast, molecules with poor solubility and a rigid planar structure, such as corticosterone, adenine, guanine, cytosine and folic acid, show a relative abundance lower than 20% (Fig. 4b).

In total, 78 of the 180 condensate-generated metabolites reported in our study (mass tolerance: ± 0.005 Da, relative error: <5.0 ppm) were not found on PubChem and the human metabolome database (HMDB). These new metabolites can be considered as heterodimers of two known metabolites linking by a C–N bond. They share structural similarity with known ones, while possessing their own unique structural features (Fig. 4c). We verified these compounds with collision-induced dissociation (CID) MS/MS analysis by matching fragmentation patterns with synthetic standards (Fig. 4d). For example, the precursor ion m/z 186.1231 (a) generated fragments at m/z 168.1138 (b) and 150.1022 (d) by consecutively losing one or two water molecules, correlating with the existence of two hydroxyl groups on the glyceraldehyde part.

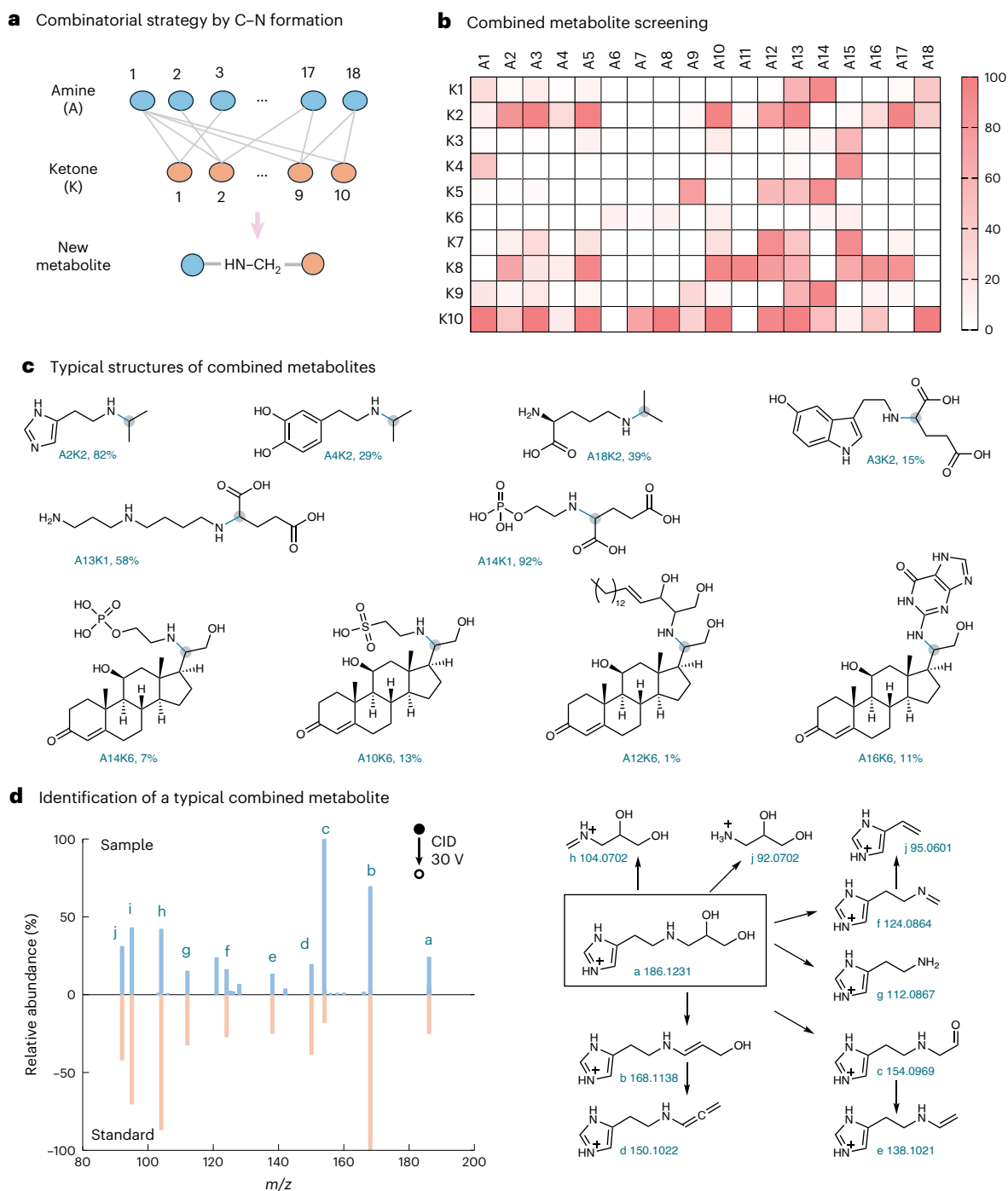


Fig. 4 | Condensate-dependent expansion of metabolite diversity by combinatory strategy. **a**, Diagram of the combinatory strategy to create new compounds linked by C–N bond to generate metabolite structural diversity. A total of 18 amine-containing metabolite species and 10 different endogenous ketones and aldehydes were used for the combinatory metabolomics study. **b**, Yields of different metabolites generated by C–N bond coupling, which are presented in a heat map. **c**, Demonstration of generated new metabolites structure linked by the C–N bond. From the point of amine modification, it can be the alkyl group, alkane-containing carboxylic group or even bulky steroid alkane-containing hydroxyl group. From the point of ketone amination,

amine species also have highly structural variability. Generally, amines with strong basicity, polarized dipoles and solubility tend to achieve higher yields. Carbonyl groups in a rigid planar structure with low solubility tend to have relatively poor yields. **d**, Identification of representative metabolites composed of histamine and glyoxylic acid. CID-MS/MS was conducted on samples containing condensates and the expected compounds obtained through organic synthesis and purification. Their spectra are in high agreement with each other. Most fragment ions can be rationally assigned to local moieties from the expected metabolite structure.

The formation of the C–N linkage was verified by the detection of fragment ions at m/z 95.0601 (i) and 92.0702 (j), which directly correlate with the structures of histamine and 3-amino-1,2-propanediol, as found by searching the HMDB. Adding up the molecular weights of these two

fragments plus one proton gives the precursor ion at m/z 186.1231, suggesting that these two structures are complementary parts of the target structure. The diverse chemistry driven by condensates further supports their role in facilitating global chemical processes.

Validation of C–N bond formation by condensates in living cells

To assess whether the ability to mediate C–N bond formation by condensates is valid in living cells, we implemented our previously demonstrated strategy to generate *Escherichia coli* cells with or without the model condensates^{54,72}, which was verified through confocal microscopy (Supplementary Fig. 12a). We then subjected the samples for untargeted metabolomics by nESI-MS (Supplementary Fig. 12b,c). Principal component analysis (PCA) was conducted to analyze the differential metabolic profiles for cells with and without condensates (Fig. 5a). We found distinct metabolic profiles between groups, which suggests the aberrant regulation of certain known metabolites or even the presence of new metabolites (Fig. 5b).

Compared to cells without condensates, there were 36 upregulated and 35 downregulated metabolites in the cell with condensates (Supplementary Table 1). Apart from these well-known metabolites, we also discovered that 23 metabolites specifically existed in the cells with condensates with statistical significance compared to the control group (Supplementary Table 2). We found that the combined new metabolites mainly derived from glucosamine (A16), glycine (A17), anthranilic acid (A15) and the addition of ammonium ion (A1) (Fig. 5c). Using the combinatorial strategy, we also predicted the existence of alkylated putrescine (A19) and 5-aminopentanoic acid (A20). The alkylation modification group could originate from nearly every type of ketone or aldehyde metabolite we previously investigated, except for corticosterone (Fig. 5d). This finding strongly agrees with our *in vitro* results. To confirm that these changes in metabolic profiles were not caused by induced protein expression, we evaluated the global metabolism of the same cell type with induced expression of a green fluorescent protein (GFP) from the same backbone of RLP at the same exponential growth phase (Supplementary Fig. 12d). We observed highly similar metabolic profiles between cells with induced GFP expression and cells without condensates (Supplementary Fig. 12e), which confirms that the global change of metabolic profiles is not related to overexpression.

It is worth noting that the levels of aspartate (A1K4), alanine (A1K5) and glucosamine were significantly increased in cells with condensates. Although these were not new metabolites, we speculate that their increases should be highly associated with the condensate-facilitated amination reaction from the corresponding ketones (that is, oxaloacetic acid, glyoxylic acid and glucose, respectively). In addition, we found two pairs of conversions that involve metabolite substrates and products in the opposite trends of changes, putrescine/*N*-carboxymethyl putrescine (A19K9) and 5-aminopentanoic acid/*N*-ethyl 5-aminopentanoic acid (A20K8). These two pairs of conversions might support the ongoing C–N coupling process or imply the coupling between the positive or negative feedback regulated by condensates and endogenous cellular pathways of living cells to realize cellular chemical homeostasis. Another interesting discovery is the decrease in reduced glutathione, which may suggest its role as a proton donor for reductive amination (Fig. 5e). These diverse chemical functions of condensates in living cells confirm their roles in regulating global chemical homeostasis.

To specifically study the intracellular capability of condensates to drive C–N formation, we generated *E. coli* strains with single-gene knockouts, $\Delta alaA$ and $\Delta argD$. The *alaA* gene encodes a glutamate-pyruvate aminotransferase, which catalyzes the reductive amination of pyruvate to form alanine, whereas *argD* encodes an arginine aminotransferase, which catalyzes the amination for arginine formation⁷³. We first cultured the knockout strains in minimum medium containing casamino acids to ensure faithful generation of condensates (Supplementary Fig. 13a). Then, we subjected the knockout strains for targeted metabolomics and found that, compared to cells without condensates, the cells containing condensates significantly restored the synthesis of alanine and arginine in their corresponding knockout

strains (Supplementary Fig. 13b). These experiments further confirm that the role of condensates in driving C–N bond formation is valid in living cells.

Lastly, to evaluate the generality of this function, we analyzed the change of global metabolism by comparing wild-type *E. coli* MG1655 with or without stress-induced condensates⁷⁴. We found that a substantially differentiated metabolism profile was observed between the two types of cells (Supplementary Fig. 14). Notably, the categories of the upregulated metabolites align with our observations in the cells containing the RLP condensates. This observation implies that the capability of condensates driving C–N bond formation in living cells is a global cellular effect and likely to be generalizable ('Discussion').

A reshaped global metabolism

To gain insight into how condensates may reshape the global metabolism, a bioinformatic analysis was conducted by summarizing all those differentially generated metabolites on the basis of metabolic pathways and function enrichment procedure⁷⁵ (Supplementary Table 3). Specifically, we found that a wide array of nitrogen metabolism pathways was influenced, such as metabolic pathways involving arginine, glycine, alanine, aspartate, glutamate and glutathione (Supplementary Fig. 15). The cells with condensates also showed notable differences in pathways associated with energy-dependent carbon metabolism and nitrogen metabolism by the urea cycle, ammonia recycling, the glucose-alanine cycle and aspartate shuttle (Supplementary Fig. 16). Specifically, upregulation of glucose and glucose 6-phosphate and downregulation of maltose and glyceraldehyde-3-phosphate indicated the boost of aerobic glycolysis for the energy fueling and diminished gluconeogenesis. Meanwhile, anaerobic glycolysis seems to be retained, which could be explained by the decrease in lactate production. Nonetheless, we noted that these energy-associated changes may be attributed to the fact that IPTG, the gene expression inducer, was added to enable condensate formation. As such, despite our analysis of the cells with or without condensates at their exponential growth stages⁷⁶, for condensate-forming cells, the gene expression process might also contribute to the consumption of cellular energy.

Interestingly, bioinformatics analysis showed the impact of condensates on interconnecting the carbon and nitrogen metabolism subregions across the whole network according to the changes in glyoxylate, pyruvate, oxaloacetate, glycine, aspartate and glutamate, which are either substrates or products of reductive amination initiated by the proposed condensate-mediated C–N coupling (Supplementary Fig. 17). Although the analysis of specific pathways supports the capability of condensates on mediating C–N bond formation, the notable alterations of global metabolism by condensates further imply the breadth of chemistry that can be affected by condensates, which emphasizes the important functional roles of establishing coexisting phases in living cells. These findings demonstrate that condensates extend beyond molecular recognition, acting as key regulators of biochemical activity at a global level.

Discussion

Understanding of cellular functions has traditionally relied on interpreting specific intermolecular interactions at the nanoscale. From an evolutionary standpoint, where simplicity and thermodynamic efficiency are largely appreciated, if the functions can be encoded at a smaller physical length scale, why would establishing coexisting phases at a micron scale be necessary for a cell, such as in the case of biomolecular condensates? Our study demonstrates that biomolecular condensates, formed by constituents lacking enzymatic activity, can serve as electrochemical reactors that can drive spontaneous C–N bond formation, a fundamental chemistry involved in diverse biochemical reactions. Unlike molecular enzymes, which typically exhibit substrate specificity because of the functions that are encoded at the nanoscale, condensates, whose enzymatic capability is defined by their

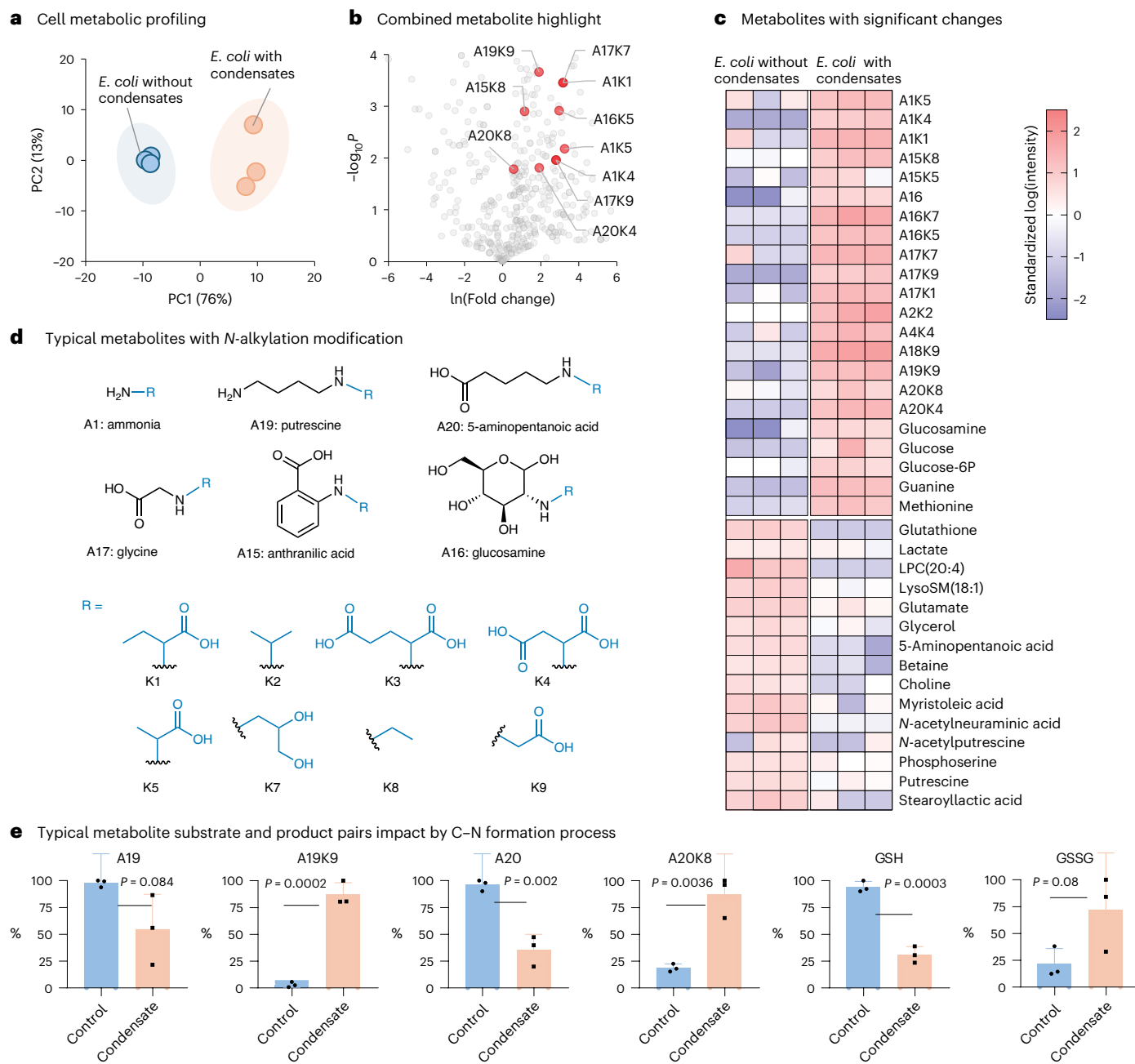


Fig. 5 | Living cell validation of condensate-dependent generation of new metabolites with metabolomics. **a**, Score plot of PCA showing the metabolic profile distribution of cells with or without condensate groups. **b**, Volcano plot displaying significantly changed metabolites. Metabolites generated from a combination of different metabolites are highlighted. Statistical analysis was performed using a two-tailed *t*-test. The FDR was calculated using the Benjamini–Hochberg procedure to reduce the false positives. **c**, Heat map of the significantly changed metabolites in cells with condensates compared with cells without condensates. Cell with or without condensates were collected at different

time points in the exponential growth stage for further analysis. The scale bar represents the log-transformed, standardized intensity of each metabolite ion in cells. **d**, Structures of representative amine metabolites and their alkylated modifications contributed by native ketone or aldehyde metabolites. **e**, Box plots of typical metabolites that were upregulated or downregulated by condensate formation in *E. coli*, where 100% represents the ion intensity normalized with the maximum value of each group. Data points represent the mean \pm s.d. ($n = 3$ biological replicates). Statistical analysis was performed using a two-tailed *t*-test.

electrochemical environments at the micron scale, can facilitate the transformation of substrates across a wide range of chemical structures. Thus, the formation of condensates likely triggers shifts in the global cellular physiology by modulating the intracellular chemical landscape.

Our study reveals the feasibility of condensate-mediated non-enzymatic C–N coupling to generate new metabolite in cells. This phenomenon can be attributed to the reactive interfacial environment and unique chemical and electrochemical environment of condensates.

From an electrochemistry aspect, the interphase possesses a differential potential on the order of tens of millivolts defined by the ion gradient between phases^{18,25}, which was recently explicitly verified through electrochemical potentiometry²⁰. Given that the width of such electric double layer is typically 5–50 nm (refs. 44,77), the oriented external electric field across the condensate interface can reach magnitudes of 10^7 – 10^9 V m⁻¹. Given the fluctuating nature of the electric field strength, such a field is sufficient to align molecular dipoles, polarize molecules

and redistribute electron density^{30,37}. From a solvent aspect, phase transition results in a unique water environment within the dense phase and at the interface^{19,29,78}, which can alter the solvation properties of substrates on the basis of their polarity. Consequently, these factors facilitate nucleophilic attack by amines onto carbonyl groups, leading to imine formation, the first step in reductive amination.

For the follow-up imine hydrogenation, our previous studies demonstrated that condensates are able to reduce resazurin through water oxidation-dependent electron transfer^{15,17,20}, generating H₂O₂ as a byproduct^{15,26,33}. This suggests that condensates are capable of providing a solvated electron to drive reduction reaction, such as imine hydrogenation. In living cells, the availability of H donors such as the reduced forms of nicotinamide adenine dinucleotide phosphate (NADPH⁺), flavin adenine dinucleotide (FADH⁺) and glutathione (GSH) may further support this reduction process. Furthermore, the strong electric field can make the system more susceptible to reduction reaction by lowering the thermodynamic barrier and enhancing the efficiency of the electron transfer process^{31,32,37,38}.

Asymmetry in phase transition is critical to define the potential gradient, which serves as the thermodynamic factor enabling the chemical activity of condensates^{17,22,23}. It is easy to understand that the charge condition of the biomacromolecule is critical to control such asymmetry. However, in theory, such asymmetry can be encoded in various factors, including chain flexibility, hydrophobicity, water density, water activity and stoichiometry of electrostatic interactions. Considering an extreme case that the phase transition protein element is neutral and mediated through hydrophobicity, such a phase transition leads to a water concentration gradient between the dilute and the dense phases, causing different spatial water activities because of the different hydrophobicity of amino acid compositions and backbones. Then, under such an environment, different types of ions possess different free energies of solvation⁷⁹ and will partition differently into the dilute and the dense phases⁸⁰. This simple process will directly induce an electric potential gradient between phases, even if the phase-separation-driving protein is charge neutral.

Another key feature that can be critical to set up an electrochemically active environment is the interfacial field. To illustrate the generality of the interfacial field, let us consider another extreme case, namely that of an insulator in a water tank. The presence of an additional surface in the water tank alters the homogeneous and isotropic nature of water molecules and forces them to align their dipoles onto the surface of the insulator⁸¹. Therefore, even without any charged elements on the surface, an oriented dipole field is established because of the asymmetric nature of the solvent at the surface^{82,83}. This dipole field, which is a part of the electric field of an interface, can also induce ion alignment, thereby mediating a double-layer structure serving as the electrostatic field. Therefore, from the basic physical chemistry aspect of phase transition and a surface¹⁷, the fundamental electrochemical properties of a phase-separated system containing a defined liquid-liquid interface should be generalizable but the exact molecular rules and mechanisms are still largely unknown.

The metabolome consists of thousands of small organic metabolites with molecular weight less than 1,000 Da (ref. 84). However, the diversity and complexity of the human metabolome make it challenging to identify and characterize every metabolite. Many metabolites have identical molecular formulas but differ in structure, functional group positioning or stereochemistry, complicating accurate identification. Furthermore, existing metabolite databases, although continuously expanding, remain incomplete, which creates difficulties in assigning definitive structures to new metabolites. Our study sheds light on these challenges by demonstrating that condensates can serve as an electrochemical reactor powering reactions between various substrates. This suggests a possible formation mechanism of those unexplored metabolites in humans, which

could account for the many unexplored or unannotated molecules in metabolomic databases.

The ability of condensates to mediate C–N bond formation across diverse substrates—ranging from endogenous metabolites such as ketones, aldehydes and amines to exogenous chemicals, demonstrates a nonenzymatic strategy for modulating anabolic reactions. This discovery suggests that, depending on the coupling between the chemical substrates and the condensate microenvironment, the inherent chemical activity of condensates might serve as a mechanism for mediating basal-level chemical distribution, maintaining cellular chemical homeostasis. For instance, through the ability of condensates to drive catabolic reactions, such as by promoting hydrolysis reactions²⁹, condensates may catalyze ATP hydrolysis to provide cellular energy; in the meantime, through the ability of condensates to synthesize nitrogen-containing and carbon-containing metabolites and reduce their degradation, condensates may contribute to nitrogen and carbon storage. These functional differences may be defined by the chemical properties of different substrates and can possibly be affected by the relative abundance of chemicals with different electrochemical potentials in unique condensate solvent environments^{85,86}. Furthermore, condensates have been proposed as a prebiotic model of living systems⁸⁷. The discovered intrinsic chemical reactivity of condensates might provide a direct connection between compartmentalization chemistry and chemical reactivity, which might largely simplify the complex requirements for prebiotic chemistry. The existence of interfacial field at condensate surface also matches the proposed criteria that enables the reconstruction of metabolic origin of life⁴⁵, which can potentially expand the chemical diversity and complexity in protometabolism^{66,88}. The coupling nature between thermodynamics and kinetics of such field-driven reactions, in which the reaction can change the thermodynamic equilibrium of the electric double layer, might serve as feedback controls to sustain chemical homeostasis.

Lastly, we propose several potential biological functions of condensate-mediated C–N formation in cells. The first is maintenance of basal chemical activity, where condensate-dependent chemistry may help stabilize cellular function by facilitating the synthesis of key metabolites and minimizing their degradation. The second is a compensatory mechanism for loss of protein function, where protein denaturation, aggregation or phase separation^{11,89,90}, which typically leads to the formation of large macromolecular assemblies, often results in loss of their chemical activities. Such condensate-dependent chemistry might serve as a backup strategy developed from natural evolution for compensating these losses by providing alternative chemical pathways. The third is adaptive response to cellular stress, whereby many condensates form in response to cellular stress. The non-selective chemical activity of condensates may serve as a self-protective mechanism against environmental disturbances, such as chemical toxicants, drugs and pollutants.

Our findings suggest that condensates have a crucial role in shaping the complexity of cellular chemistry. By driving nonenzymatic C–N bond formation, condensates extend beyond traditional biochemical paradigms, transforming our understanding of cellular metabolic pathways. More broadly, our work emphasizes the importance of micron-sized physical structures in defining the chemical capabilities of living cells. These insights open new avenues for studying cellular biochemistry, particularly the interplay between biomolecular condensates and nonenzymatic metabolic regulation.

Online content

Any methods, additional references, Nature Portfolio reporting summaries, source data, extended data, supplementary information, acknowledgements, peer review information; details of author contributions and competing interests; and statements of data and code availability are available at <https://doi.org/10.1038/s41589-026-02169-2>.

References

1. Brangwynne, C. P. et al. Germline P granules are liquid droplets that localize by controlled dissolution/condensation. *Science* **324**, 1729–1732 (2009).
2. Shin, Y. & Brangwynne, C. P. Liquid phase condensation in cell physiology and disease. *Science* **357**, eaaf4382 (2017).
3. Choi, J.-M., Holehouse, A. S. & Pappu, R. V. Physical principles underlying the complex biology of intracellular phase transitions. *Annu. Rev. Biophys.* **49**, 107–133 (2020).
4. Lyon, A. S., Peeples, W. B. & Rosen, M. K. A framework for understanding the functions of biomolecular condensates across scales. *Nat. Rev. Mol. Cell Biol.* **22**, 215–235 (2021).
5. Banani, S. F., Lee, H. O., Hyman, A. A. & Rosen, M. K. Biomolecular condensates: organizers of cellular biochemistry. *Nat. Rev. Mol. Cell Biol.* **18**, 285–298 (2017).
6. Alberti, S. & Hyman, A. A. Biomolecular condensates at the nexus of cellular stress, protein aggregation disease and ageing. *Nat. Rev. Mol. Cell Biol.* **22**, 196–213 (2021).
7. Dai, Y., You, L. & Chilkoti, A. Engineering synthetic biomolecular condensates. *Nat. Rev. Bioeng.* **1**, 466–480 (2023).
8. Tsang, B., Pritišanac, I., Scherer, S. W., Moses, A. M. & Forman-Kay, J. D. Phase separation as a missing mechanism for interpretation of disease mutations. *Cell* **183**, 1742–1756 (2020).
9. Lasker, K. et al. Selective sequestration of signalling proteins in a membraneless organelle reinforces the spatial regulation of asymmetry in *Caulobacter crescentus*. *Nat. Microbiol.* **5**, 418–429 (2020).
10. Ray, P. S., Arif, A. & Fox, P. L. Macromolecular complexes as depots for releasable regulatory proteins. *Trends Biochem. Sci.* **32**, 158–164 (2007).
11. Michaels, T. C. T. et al. Amyloid formation as a protein phase transition. *Nat. Rev. Phys.* **5**, 379–397 (2023).
12. Falahati, H. & Haji-Akbari, A. Thermodynamically driven assemblies and liquid–liquid phase separations in biology. *Soft Matter* **15**, 1135–1154 (2019).
13. Tadros, T. in *Colloid Stability: The Role of Surface Forces—Part 1* (ed. Tadros, T.) Ch. 1 (Wiley, 2007).
14. Stol, R. & DeBruyn, P. Thermodynamic stabilization of colloids. *J. Colloid Interface Sci.* **75**, 185–198 (1980).
15. Dai, Y. et al. Interface of biomolecular condensates modulates redox reactions. *Chem* **9**, 1594–1609 (2023).
16. Watson, J. L. et al. Macromolecular condensation buffers intracellular water potential. *Nature* **623**, 842–852 (2023).
17. Dai, Y., Wang, Z.-G. & Zare, R. N. Unlocking the electrochemical functions of biomolecular condensates. *Nat. Chem. Biol.* **20**, 1420–1433 (2024).
18. Posey, A. E. et al. Biomolecular condensates are characterized by interphase electric potentials. *J. Am. Chem. Soc.* **146**, 28268–28281 (2024).
19. Ye, S. et al. Micropolarity governs the structural organization of biomolecular condensates. *Nat. Chem. Biol.* **20**, 443–453 (2023).
20. Yu, W. et al. Aging-dependent evolving electrochemical potentials of biomolecular condensates regulate their physicochemical activities. *Nat. Chem.* **17**, 756–766 (2025).
21. Shen, K. & Wang, Z.-G. Polyelectrolyte chain structure and solution phase behavior. *Macromolecules* **51**, 1706–1717 (2018).
22. Zhang, P. & Wang, Z.-G. Interfacial structure and tension of polyelectrolyte complex coacervates. *Macromolecules* **54**, 10994–11007 (2021).
23. Zhang, P., Alsaifi, N. M., Wu, J. & Wang, Z.-G. Polyelectrolyte complex coacervation: effects of concentration asymmetry. *J. Chem. Phys.* **149**, 163303 (2018).
24. Zhang, P., Alsaifi, N. M., Wu, J. & Wang, Z.-G. Salting-out and salting-in of polyelectrolyte solutions: a liquid-state theory study. *Macromolecules* **49**, 9720–9730 (2016).
25. Hoffmann, C. et al. Electric potential at the interface of membraneless organelles gauged by graphene. *Nano Lett.* **23**, 10796–10801 (2023).
26. Chen, M. W. et al. Transition-state-dependent spontaneous generation of reactive oxygen species by A β assemblies encodes a self-regulated positive feedback loop for aggregate formation. *J. Am. Chem. Soc.* **147**, 8267–8279 (2025).
27. Eisenthal, K. B. Second harmonic spectroscopy of aqueous nano- and microparticle interfaces. *Chem. Rev.* **106**, 1462–1477 (2006).
28. Lee, H. J., Jamison, A. C. & Lee, T. R. Surface dipoles: a growing body of evidence supports their impact and importance. *Acc. Chem. Res.* **48**, 3007–3015 (2015).
29. Guo, X. et al. Biomolecular condensates can function as inherent catalysts. Preprint in *bioRxiv* <https://doi.org/10.1101/2024.07.06.602359> (2024).
30. Shi, L. et al. Water structure and electric fields at the interface of oil droplets. *Nature* **640**, 87–93 (2025).
31. Shaik, S., Danovich, D., Joy, J., Wang, Z. & Stuyver, T. Electric-field mediated chemistry: uncovering and exploiting the potential of (oriented) electric fields to exert chemical catalysis and reaction control. *J. Am. Chem. Soc.* **142**, 12551–12562 (2020).
32. LaCour, R. A., Heindel, J. P., Zhao, R. & Head-Gordon, T. The role of interfaces and charge for chemical reactivity in microdroplets. *J. Am. Chem. Soc.* **147**, 6299–6317 (2025).
33. Yan, X. et al. Intra-condensate demixing of TDP-43 inside stress granules generates pathological aggregates. *Cell* **188**, 4123–4140 (2025).
34. Hu, K., Relton, E., Locker, N., Phan, N. T. & Ewing, A. G. Electrochemical measurements reveal reactive oxygen species in stress granules. *Angew. Chem. Int. Ed. Engl.* **60**, 15302–15306 (2021).
35. Abbas, M., Lipiński, W. P., Nakashima, K. K., Huck, W. T. S. & Spruijt, E. A short peptide synthon for liquid–liquid phase separation. *Nat. Chem.* **13**, 1046–1054 (2021).
36. Harris, R., Berman, N. & Lampel, A. Coacervates as enzymatic microreactors. *Chem. Soc. Rev.* **54**, 4183–4199 (2025).
37. Shaik, S., Mandal, D. & Ramanan, R. Oriented electric fields as future smart reagents in chemistry. *Nat. Chem.* **8**, 1091–1098 (2016).
38. Wang, Z., Danovich, D., Ramanan, R. & Shaik, S. Oriented-external electric fields create absolute enantioselectivity in Diels–Alder reactions: importance of the molecular dipole moment. *J. Am. Chem. Soc.* **140**, 13350–13359 (2018).
39. Li, J., Zhang, Y., Kuruvinashetti, K. & Kornienko, N. Construction of C–N bonds from small-molecule precursors through heterogeneous electrocatalysis. *Nat. Rev. Chem.* **6**, 303–319 (2022).
40. Hili, R. & Yudin, A. K. Making carbon–nitrogen bonds in biological and chemical synthesis. *Nat. Chem. Biol.* **2**, 284–287 (2006).
41. Alberts, B. et al. *Molecular Biology of the Cell* 7th edn (WW Norton & Company, 2017).
42. Warshel, A. et al. Electrostatic basis for enzyme catalysis. *Chem. Rev.* **106**, 3210–3235 (2006).
43. Fried, S. D., Bagchi, S. & Boxer, S. G. Extreme electric fields power catalysis in the active site of ketosteroid isomerase. *Science* **346**, 1510–1514 (2014).
44. Suydam, I. T., Snow, C. D., Pande, V. S. & Boxer, S. G. Electric fields at the active site of an enzyme: direct comparison of experiment with theory. *Science* **313**, 200–204 (2006).
45. Zimmermann, J., Werner, E., Sodei, S. & Moran, J. Pinpointing conditions for a metabolic origin of life: underlying mechanisms and the role of coenzymes. *Acc. Chem. Res.* **57**, 3032–3043 (2024).
46. Chen, B. et al. Water–solid contact electrification causes hydrogen peroxide production from hydroxyl radical recombination in sprayed microdroplets. *Proc. Natl Acad. Sci. USA* **119**, e2209056119 (2022).

47. Xiong, H., Lee, J. K., Zare, R. N. & Min, W. Strong electric field observed at the interface of aqueous microdroplets. *J. Phys. Chem. Lett.* **11**, 7423–7428 (2020).
48. Lee, J. K. et al. Spontaneous generation of hydrogen peroxide from aqueous microdroplets. *Proc. Natl Acad. Sci. USA* **116**, 19294–19298 (2019).
49. Song, X., Basheer, C. & Zare, R. N. Making ammonia from nitrogen and water microdroplets. *Proc. Natl Acad. Sci. USA* **120**, e2301206120 (2023).
50. Berbille, A. et al. Mechanism for generating H₂O₂ at water–solid interface by contact-electrification. *Adv. Mater.* **35**, 2304387 (2023).
51. Wang, Z. et al. Contact-electro-catalysis for the degradation of organic pollutants using pristine dielectric powders. *Nat. Commun.* **13**, 130 (2022).
52. Galembeck, F., Santos, L. P., Burgo, T. A. L. & Galembeck, A. The emerging chemistry of self-electrified water interfaces. *Chem. Soc. Rev.* **53**, 2578–2602 (2024).
53. Dzuricky, M., Rogers, B. A., Shahid, A., Cremer, P. S. & Chilkoti, A. De novo engineering of intracellular condensates using artificial disordered proteins. *Nat. Chem.* **12**, 814–825 (2020).
54. Dai, Y. et al. Programmable synthetic biomolecular condensates for cellular control. *Nat. Chem. Biol.* **19**, 518–528 (2023).
55. Murakami, T. et al. ALS/FTD mutation-induced phase transition of FUS liquid droplets and reversible hydrogels into irreversible hydrogels impairs RNP granule function. *Neuron* **88**, 678–690 (2015).
56. Brady, J. P. et al. Structural and hydrodynamic properties of an intrinsically disordered region of a germ cell-specific protein on phase separation. *Proc. Natl Acad. Sci. USA* **114**, E8194–E8203 (2017).
57. Bremer, A. et al. Deciphering how naturally occurring sequence features impact the phase behaviours of disordered prion-like domains. *Nat. Chem.* **14**, 196–207 (2022).
58. Nott, T. J. et al. Phase transition of a disordered nuage protein generates environmentally responsive membraneless organelles. *Mol. Cell* **57**, 936–947 (2015).
59. Ambadi Thody, S. et al. Small-molecule properties define partitioning into biomolecular condensates. *Nat. Chem.* **16**, 1794–1802 (2024).
60. Ruiz-Lopez, M. F., Francisco, J. S., Martins-Costa, M. T. C. & Anglada, J. M. Molecular reactions at aqueous interfaces. *Nat. Rev. Chem.* **4**, 459–475 (2020).
61. Afanasyev, O. I., Kuchuk, E., Usanov, D. L. & Chusov, D. Reductive amination in the synthesis of pharmaceuticals. *Chem. Rev.* **119**, 11857–11911 (2019).
62. Lyklema, J. (ed.) *Fundamentals of Interface and Colloid Science: Soft Colloids* Vol. 5 (Elsevier, 2005).
63. Perrin, D. D. *Ionisation Constants of Inorganic Acids and Bases in Aqueous Solution* 2nd edn (Elsevier, 2016).
64. Scheller, P. N. et al. Enzyme toolbox: novel enantiocomplementary imine reductases. *ChemBioChem* **15**, 2201–2204 (2014).
65. Su, X., Wellen, K. E. & Rabinowitz, J. D. Metabolic control of methylation and acetylation. *Curr. Opin. Chem. Biol.* **30**, 52–60 (2016).
66. Muchowska, K. B., Varma, S. J. & Moran, J. Nonenzymatic metabolic reactions and life's origins. *Chem. Rev.* **120**, 7708–7744 (2020).
67. Abraham, A. K. & Pihl, A. Role of polyamines in macromolecular synthesis. *Trends Biochem. Sci.* **6**, 106–107 (1981).
68. Kumar, A., Taylor, M., Altabella, T. & Tiburcio, A. F. Recent advances in polyamine research. *Trends Plant Sci.* **2**, 124–130 (1997).
69. Heby, O. & Persson, L. Molecular genetics of polyamine synthesis in eukaryotic cells. *Trends Biochem. Sci.* **15**, 153–158 (1990).
70. Wang, J. et al. A molecular grammar governing the driving forces for phase separation of prion-like RNA binding proteins. *Cell* **174**, 688–699 (2018).
71. Nott, T. J., Craggs, T. D. & Baldwin, A. J. Membraneless organelles can melt nucleic acid duplexes and act as biomolecular filters. *Nat. Chem.* **8**, 569–575 (2016).
72. Dai, Y. et al. Biomolecular condensates regulate cellular electrochemical equilibria. *Cell* **187**, 5951–5966 (2024).
73. Wu, G. Amino acids: metabolism, functions, and nutrition. *Amino Acids* **37**, 1–17 (2009).
74. Jin, X. et al. Membraneless organelles formed by liquid-liquid phase separation increase bacterial fitness. *Sci. Adv.* **7**, eabn2929 (2021).
75. Pang, Z. et al. MetaboAnalyst 5.0: narrowing the gap between raw spectra and functional insights. *Nucleic Acids Res.* **49**, W388–W396 (2021).
76. Andersen, K. B. & von Meyenburg, K. Are growth rates of *Escherichia coli* in batch cultures limited by respiration? *J. Bacteriol.* **144**, 114–123 (1980).
77. Fried, S. D. & Boxer, S. G. Measuring electric fields and noncovalent interactions using the vibrational Stark effect. *Acc. Chem. Res.* **48**, 998–1006 (2015).
78. Joshi, A. et al. Hydrogen-bonded network of water in phase-separated biomolecular condensates. *J. Phys. Chem. Lett.* **15**, 7724–7734 (2024).
79. Hummer, G., Pratt, L. R. & Garcia, A. E. Free energy of ionic hydration. *J. Phys. Chem.* **100**, 1206–1215 (1996).
80. Yang, L., Yu, W., Zeng, X. & Dai, Y. Asymmetry in hydrophobicity induces electric potential in non-charged biomolecular condensates. *Adv. Sci.* <https://doi.org/10.1002/adv.202524324> (2026).
81. Israelachvili, J. N. *Intermolecular and Surface Forces* 3rd edn (Academic Press, 2011).
82. Björneholm, O. et al. Water at interfaces. *Chem. Rev.* **116**, 7698–7726 (2016).
83. Gonella, G. et al. Water at charged interfaces. *Nat. Rev. Chem.* **5**, 466–485 (2021).
84. Patti, G. J., Yanes, O. & Siuzdak, G. Metabolomics: the apogee of the omics trilogy. *Nat. Rev. Mol. Cell Biol.* **13**, 263–269 (2012).
85. Marcus, R. A. in *Protein Electron Transfer* (ed. Bendall, D.) Ch. 10 (Garland Science, 2020).
86. Bard, A. J., Faulkner, L. R. & White, H. S. *Electrochemical Methods: Fundamentals and Applications* 3rd edn (Wiley, 2022).
87. Ren, X. et al. Anion- π interaction-induced phase separation as a prebiotic pathway to oxygenation. *Proc. Natl Acad. Sci. USA* **122**, e2508804122 (2025).
88. Kaur, H. et al. A prebiotic Krebs cycle analog generates amino acids with H₂ and NH₃ over nickel. *Chem* **10**, 1528–1540 (2024).
89. Riback, J. A. et al. Stress-triggered phase separation is an adaptive, evolutionarily tuned response. *Cell* **168**, 1028–1040 (2017).
90. Franzmann, T. M. et al. Phase separation of a yeast prion protein promotes cellular fitness. *Science* **359**, eaao5654 (2018).

Publisher's note Springer Nature remains neutral with regard to jurisdictional claims in published maps and institutional affiliations.

Springer Nature or its licensor (e.g. a society or other partner) holds exclusive rights to this article under a publishing agreement with the author(s) or other rightsholder(s); author self-archiving of the accepted manuscript version of this article is solely governed by the terms of such publishing agreement and applicable law.

© The Author(s), under exclusive licence to Springer Nature America, Inc. 2026

Methods

Protein purification of RLP

E. coli BL21 (DE3) cells were transformed with the RLP_{WT} gene⁵⁴ and selected on kanamycin plates. A single colony was picked and cultured overnight in 4 ml of 2×YT medium containing 50 μg ml⁻¹ kanamycin and 2% glucose at 37 °C with shaking at 250 rpm. The overnight culture was then diluted into 1 L of 2×YT medium containing 50 μg ml⁻¹ kanamycin and incubated at 37 °C with shaking at 250 rpm for 3 h. Induction of protein expression was achieved by adding IPTG to a final concentration of 0.5 mM, followed by overnight incubation at 37 °C with continuous shaking. Then, 800 ml of cells were harvested by centrifugation at 3,500g for 10 min at 4 °C (Eppendorf High-Speed Centrifuge, CR22N). The cell pellet was then resuspended in 35 ml of lysis buffer (50 mM Tris pH 7.5). Cell solutions were lysed by sonication on ice (2 min of sonication with 1 s on and 2 s off at 30% intensity). After centrifuging the cell lysate at 15,000g for 30 min at 4 °C to separate the soluble and insoluble fractions, the insoluble pellet was reconstituted in 10 ml of urea buffer (50 mM Tris, 500 mM NaCl and 4 M urea, pH 7.5) and treated with 500 U of Benzonase nuclease (MilliporeSigma) in a water bath at 40 °C for a minimum of 2 h. The protein sample was subsequently heated to 40 °C and centrifuged again at 15,000g for 30 min at 40 °C. The resulting supernatant was collected and subjected to dialysis against 50 mM Tris buffer pH 7.5 for 3 h. Following dialysis, the solution underwent centrifugation at 15,000g for 30 min at 4 °C. The pellet, containing the RLP protein, was redissolved in buffer (50 mM Tris, 500 mM NaCl and 4 M urea, pH 7.5) and incubated for 2 h at 40 °C. After this, the dissolved protein was centrifuged at 15,000g for 30 min at 40 °C. The supernatant was then dialyzed once more into 50 mM Tris buffer pH 7.5 for 3 h. The soluble and insoluble phases within the dialysis bag were harvested and subsequently centrifuged at 15,000g for 30 min at 4 °C. The pellet was redissolved in urea buffer (50 mM Tris, 500 mM NaCl and 4 M urea, pH 7.5) and incubated at 40 °C for 2 h. The solution was centrifuged at 15,000g for 30 min at 40 °C and the purity of the supernatant was evaluated using SDS-PAGE with Bio-Rad's any kD Mini-PROTEAN TGX precast protein gels. This procedure concluded one cycle of purification for upper critical solution temperature proteins. One additional cycle of temperature-dependent purification was carried out before the protein was further purified using the AKTA Pure chromatography system (Cytiva) equipped with a size-exclusion column (Superdex Increase 75). The RLP protein was diluted to below 100 μM with urea buffer and dialyzed into a buffer containing 50 mM Tris and 500 mM NaCl (pH 7.5) at room temperature, with the dialysis buffer exchanged three times over a 4-h period. Finally, the protein solution was divided into PCR tubes and frozen at -80 °C for storage.

Incubation of biomolecular condensate with substrates

To form RLP condensates, a frozen stock of the protein was thawed at room temperature just before use. For the condensate formation condition, each sample consisted of 30 μl of protein stock mixed with 70 μl of dilution buffer (50 mM Tris pH 7.5). The protein solutions were then incubated at room temperature for 30 min to allow the condensates to form. Thereafter, 1 μl of a concentrated metabolite mixture solution (100× final concentration) was spiked into either 100 μl of solution containing biomolecular condensates or a negative control solution containing the buffer alone. This volume of preparation can be scaled as wished, with the ratio of protein, dilution buffer and reactant at 30:70:1 (v/v/v) to allow the protein to phase-separate. The protein stock cannot go through multiple freeze-thaw cycles and it needs to be used immediately after thawing. For each single-metabolite substrate, a stock solution at a concentration of 5 mM was prepared in deionized water (Fisher, high-performance LC grade).

Combinatorial metabolomics

We selected α-ketobutyric acid (K1), acetone (K2), α-ketoglutaric acid (K3), oxaloacetic acid (K4), pyruvic acid (K5), corticosterone (K6),

glyceraldehyde (K7), acetaldehyde (K8), glyoxylic acid (K9) and formaldehyde (K10) as representative carbonyl species. The metabolites containing an amine group included ammonia (A1), histamine (A2), serotonin (5-hydroxytryptamine, A3), dopamine (A4), lysine (A5), adenine (A6), cytosine (A7), guanine (A8), thiamine (A9), taurine (A10), folic acid (A11), sphingosine (A12), spermidine (A13), *O*-phosphorylethanolamine (A14), anthranilic acid (A15), glucosamine (A16), glycine (A17) and ornithine (A18). Later in the nontarget cell metabolomics study, we coded the putrescine and 5-aminopentanoic acid as A19 and A20 because we successfully predicted existences of the alkylated metabolites from these two amine-containing metabolites. For each metabolite, a stock solution of 50 mM was first prepared. Then, any one of the amine standards (A_x, where x = 1–18) and any one of the carbonyl species (K_y, y = 1–10) was mixed with an equal volume ratio to form the 25 mM mixture. Thereafter, the mixed solutions containing the same amine group were pooled (concentration around 2.5 mM) and 1 μl of the combined solution was aspirated into 100 μl of buffer solution containing biomolecular condensate for incubation and reductive amination reaction (final concentration: 25 μM).

nESI-MS data acquisition

nESI-MS was used to conduct both target metabolite detection and nontarget metabolomics. The nESI sprayer tip was fabricated of borosilicate glass capillary (outer diameter, 1.5 mm; inner diameter, 0.86 mm; length, 10 cm) by placing it into a micropipette puller (Sutter P1000 Instrument). Key parameters of the pulling program were as follows: heat, 710; velocity, 15; pull, blank; time, 250; pressure, 700. A microloader (K2080231, 20 μl, Eppendorf) was used to transport 7 μl of sample solution into the nESI micropipette. A stainless-steel needle connected with a high-voltage supplier was then inserted from the back end of the micropipette into the loaded sample solution. The whole nESI tip was positioned in front of a MS instrument inlet at the distance of 3.0 mm. A high-resolution linear trap quadrupole Orbitrap Velos MS instrument (Thermo Fisher Scientific) is coupled to the nESI for data recording detection. When a +1.8 kV high voltage is applied to the needle, the strong electric field on the nESI sprayer tip will induce the spraying process for ion signal monitoring by MS. The MS capillary temperature was set at 300 °C, with an S-lens voltage of 55 V and maximum injection time set at 400 ms. The MS instrument was calibrated before measurement using ion mass calibration solution kits (Pierce positive, Thermo Fisher).

Preparation of cells with or without RLP condensates

BL21 (DE3) competent *E. coli* (New England Biolabs) was transformed with plasmid containing the RLP_{WT} gene or blank plasmid (negative control) and the transformed cells were selected by plating with 45 μg ml⁻¹ kanamycin on a 2×YT agar plate. A single colony was picked and grown overnight in minimal M9 medium (prepared by adding M9 salts with 2 mM MgSO₄, 100 μM CaCl₂ and 1% w/v glucose), supplied with 45 μg ml⁻¹ kanamycin, at 37 °C with shaking at 250 rpm. Then, 40 μl of overnight cell culture was backdiluted into 4 ml of minimal M9 medium supplied with 45 μg ml⁻¹ kanamycin. To prepare cells with condensates, when the optical density at 600 nm (OD₆₀₀) of cell culture reached 0.3, 0.5 mM IPTG was added into the culture to induce the production of the protein. The cell culture was continuously incubated at 37 °C with shaking at 250 rpm for an additional 3 h. To prepare cells without condensates, the backdiluted cells were cultured for 2 h at 37 °C without the addition of inducer. The induced cells were finally collected by centrifugation at 2,000g for 10 min at 4 °C and flash-frozen by liquid nitrogen and prepared for metabolism analysis.

Preparation of knockout strains

To construct a BL21(DE3) variant with genomic *argD* or *alaA* knocked out, plasmids were constructed by inserting the corresponding guide RNA (gRNA) sequence and the template with 500-bp homologous arms

flanking the loci into the backbone. BL21(DE3) was transformed with pMYF44 and grown on 2×YT agar with 45 μg ml⁻¹ kanamycin at 37 °C overnight. Then, 3 ml of 2×YT with 45 μg ml⁻¹ kanamycin was inoculated with a single colony and grown overnight at 37 °C with shaking at 250 rpm. The overnight culture was diluted 50-fold into 25 ml of 2×YT with 45 μg ml⁻¹ kanamycin and 1% arabinose in a 250-ml shake flask and grown at 37 °C with shaking at 250 rpm until the OD₆₀₀ was 0.35–0.4. The cells were harvested and prepared for transformation by electroporation. Competent cells were transformed with 300 ng of knockout plasmids and recovered in 600 μl of SOC medium for 2 h at 37 °C with shaking at 250 rpm. Following recovery, cells were plated on 2×YT agar supplied with 45 μg ml⁻¹ kanamycin and 34 μg ml⁻¹ chlorophenol plates and grown overnight at 37 °C. Successful knockout strains were confirmed by colony PCR. For plasmid curing, knockout plasmids were cured by growing a single colony in 3 ml of 2×YT with 45 μg ml⁻¹ kanamycin and 1% rhamnose at 37 °C with shaking at 250 rpm to induce the expression of a gRNA targeting the pBR322 origin. That culture was then plated onto 2×YT plates with no antibiotics and grown at 42 °C to cure out pMYF44.

Preparation of gene-knockout cells with or without condensates

The gene-knockout BL21 (DE3) competent *E. coli* was transformed with plasmid containing the RLP gene or blank plasmid (negative control) and the transformed cells were selected by plating with 45 μg ml⁻¹ kanamycin on a 2×YT agar plate. A single colony was picked and grown overnight in M9 medium (M9 salts with 2 mM MgSO₄, 100 μM CaCl₂, 1% w/v glucose and 0.01% casamino acids), supplied with 45 μg ml⁻¹ kanamycin, at 37 °C with shaking at 250 rpm. Then, 40 μl of overnight cell culture was backdiluted into 4 ml of M9 medium supplied with 45 μg ml⁻¹ kanamycin. To prepare cells with condensates, when the OD₆₀₀ of cell culture reached 0.3, 0.5 mM IPTG was added into the culture to induce the production of the protein. The cell culture was continuously incubated at 37 °C with shaking at 250 rpm for an additional 3 h. To prepare cells without condensates, the backdiluted cells were cultured for 2 h at 37 °C without the addition of inducer. To evaluate the extent of catalytic performance in metabolic pathways through condensate formation, BL21(DE3)-*ΔalaA* cultures were supplemented with 1 mM α-L-pyruvate, while BL21(DE3)-*ΔargD* cultures were supplemented with 1 mM L-glutamate. The induced cells were finally collected by centrifugation at 2,000g for 10 min at 4 °C, flash-frozen using liquid nitrogen and prepared for metabolism analysis.

Preparation of MG1655 stress-induced condensates

A single colony of MG1655 was cultured in M9 minimal medium overnight. Overnight cultures were backdiluted 1:100 in M9 minimal medium. For the cells without condensates, the cells were cultured for 3 h for characterization. For the formation of heat-stress-induced condensates, cells were cultured for an additional 2 h and subjected to heat shock at 48 °C for 1 h on a benchtop dry bath incubator. Cells were pelleted and resuspended into Hanks' balanced salt solution for further characterization.

Untargeted metabolomics data processing

Batches of raw MS data files were first converted to cdf format using Xcalibur software (Thermo Fisher Scientific). Then, the cdf files were imported into MATLAB2025a (Mathworks) for further data preprocessing using the in-built functions and self-programmed scripts. Briefly, each cells sample's average mass spectrum was constructed on the basis of ten continuous scans in the corresponding time window. The metabolite ion's exact *m/z* value within a ±0.005 Da tolerance was defined as a mass bin for peak intensity extraction. Lastly, a data matrix composed of peak intensities from all samples was constructed for univariate and multivariate analysis.

Statistical analysis

For multivariate analysis, SIMCA-P (Umetrics) was used for PCA of metabolic profiles. Univariate analysis was then conducted to search for significantly changed metabolite ions among model and control groups using Student's *t*-test and *F*-test. The *P* values were adjusted with the false discovery rate (FDR) using the Benjamini–Hochberg method. Data were visualized using GraphPad Prism and Microsoft Excel through heat maps, box plots, volcano plots, etc.

Identification of predicted metabolites

An ion of predicted structure was searched through HMDB (<http://hmdb.ca>) with the mass tolerance set at 5.0 ppm. The types of ion adducts were limited to [M + H]⁺, [M + Na]⁺, [M + K]⁺ and [M + 2Na - H]⁺ in positive mode. The isotope distribution was also used to rule out impossible formulas in the candidate list provided by the search engine. CID-MS/MS was conducted to get more detailed structural information. The CID fragmentation pattern of a new metabolite detected in cell was compared to the spectrum acquired from the organic synthesis product. The collision energy was tuned from 20 to 40 eV to get a good MS/MS spectrum with observable precursor ion and sufficient fragment ions. The maximum injection time was set at 400 ms with three microscans to average each spectrum.

LC-MS

Reaction samples of guanine and acetone under various incubation conditions were analyzed by LC-MS on the Waters Acquity UPLC and Thermo Exploris 240 Orbitrap MS instrument. The mobile phase consists of water containing 0.1% formic acid (solution A) and acetonitrile containing 0.1% formic acid (solution B). The elution gradient of solution B was as follows: (1) 0–95% within 0–5 min; (2) hold at 95% for 5–7 min; (3) decrease to 0% over 7–8 min; (4) hold at 0% until 15 min. The flow rate was 0.2 ml min⁻¹. A hydrophilic interaction LC column (Phenomenex Luna 100-Å PFP; inner diameter: 2.1 mm, length: 150 mm, particle size: 3 μm) was used for chromatographic separation and maintained at room temperature. The injection volume was 3 μl. Mass spectra were collected in full-scan MS mode with polarity switching and a mass range of 40–600 Da (collecting scans alternating between positive and negative ionization potentials). The Orbitrap mass resolution was set at 120,000. All samples went through protein precipitation before formal LC-MS injection. Acetonitrile was used as the protein precipitation solvent. The volume of organic solvent was 100 μl per equal volume of raw biological sample.

Fluorescence spectroscopy

A fluorometer (HORIBA Fluorolog 3-22 system) was used to collect the fluorescence emission spectra and the specific maximum emission wavelengths of amine and ketone substrates, their imine intermediates and final reductive amination products. The excitation wavelength was set at 405 nm. The monitored range of emission wavelength was from 420 nm to 650 nm with the step width at 1 nm. *N,N*-dimethyl-6-propionyl-2-naphthylamine (substrate A) and 4-amino-1,8-naphthalimide (substrate B) were selected as the model amine and ketone, respectively. Substrates A and B were both dissolved in water at a concentration of 500 μM. Equal volumes of two substrate solutions were mixed to achieve a concentration of 250 μM. A 0.1-ml aliquot of the reaction mixture was tested immediately using 4.9 ml of dilution buffer (50 mM Tris pH 7.5) to achieve a final concentration of around 5 μM. The imine intermediate's spectrum was acquired by using another aliquot of reactant mixture after 4 h of incubation under the same dilution fold. To get the spectrum of the reductive amination product, the amine intermediate was reduced by adding 100 μl of a sodium borohydride (2 mM) solution into 100 μl of reaction mixture (substrates A and B at 250 μM) for 4 h of reduction. The maximum emission wavelengths of substrates A and B were confirmed to be 450 nm and 530 nm, respectively. With the incubation time going, the emission

intensity at 450 nm was depleted and the emission at 560 nm was gradually enhanced because of the Förster resonance energy transfer effect, indicating occurrence of the condensation process and formation of the imine intermediate. The maximum emission wavelength shifted from 530 nm to 560 nm because of C–N bond formation, where the substrate A-derived electron donor group narrowed the substrate B's energy gap and consequently lowered the excitation and emission energy. Thus, 450 nm and 560 nm were selected as references to characterize the reductive amination process in the confocal microscopy test.

Condensate concentration-dependent reductive amination test

The concentration of RLP stock solution was 75 μM . A dilution series of RLP solutions was then prepared by adding 0, 2, 5, 10, 20, 25 and 30 μl of RLP stock solution into 30, 28, 25, 20, 10, 5 and 0 μl of control buffer (500 mM NaCl and 50 mM Tris, pH 7.5) for a total volume of 30 μl in each case. Thereafter, each 30- μl protein solution was mixed with 70 μl of dilute buffer (50 mM Tris pH 7.5) and incubated for 1 h. Then, equal volumes of guanine (2.5 μl , 200 μM) and acetone (2.5 μl , 200 μM) were mixed and added into 100 μl of protein buffer solution for a 5-h reaction before nESI-MS detection. The relative abundance and conversion rate were estimated as follows:

$$\text{Relative abundance \%} = 100 \times \frac{\sum I_p}{\sum I_p + \sum I_s}$$

$$\text{Conversion rate} = \frac{C_0 \times Y\%}{t}$$

Here, I_p and I_s represent the sums of the product-related and substrate-related ion intensities, respectively. The yield was estimated by presuming a close ionization efficiency between the substrate guanine and product *N*-isopropylguanine. C_0 represents the initial concentration of guanine in the protein-containing buffer solution (5 μM) and t represents the reaction time (5 h).

Purification of FUS, TAF15, EWSR1 and DDX4-LCD

The production of FUS, TAF15 and EWSR1 followed previous established protocols with slight modification⁷⁰. All constructs were expressed in Sf9 insect cells and harvested 72 h after infection. Cells were collected by centrifugation at 300g for 5 min and the resulting pellets were resuspended in lysis buffer (50 mM Tris, 1 M KCl, 5% glycerol and 10 mM imidazole, pH 7.4). Before cell lysis, a protease inhibitor cocktail was supplemented, including 1 mM PMSF, 100 μM AEBSF, 0.08 μM aprotinin, 5 μM bestatin, 1.5 μM E-64, 2 μM leupeptin and 1 μM pepstatin A. Cells were lysed by sonication, and the crude was clarified by centrifugation at 20,000g for 20 min. The supernatant was incubated with Ni-NTA agarose resin for 1 h at 4 °C. Following incubation, the resin was collected by centrifugation at 300g for 5 min and transferred into gravity flow columns. The columns were washed with three column volumes of the lysis buffer to remove nonspecifically bound proteins. Bound proteins were eluted using the elution buffer (50 mM Tris, 1 M KCl, 5% glycerol and 500 mM imidazole, pH 7.4). The eluted protein was subsequently applied to an amylose resin column and the flowthrough was collected and concentrated. Final purification was carried out by size-exclusion chromatography, using a buffer composed of 50 mM Tris pH 7.4 and 500 mM KCl. Peak fractions were pooled, aliquoted into PCR tubes, flash-frozen in liquid nitrogen and stored at –80 °C.

The production of DDX4-LCD was conducted in *E. coli* cells following a previously established protocol without modification⁷¹.

Formation of biomolecular condensates by FUS, TAF15, EWSR1 and DDX4-LCD

All stock solutions of FUS, TAF15 and EWSR1 were thawed at room temperature before use. To induce biomolecular condensate formation,

3 μl of each protein stock was mixed with 14.5 μl of dilution buffer (containing 50 mM Tris and 500 mM KCl, pH 7.4) and 2.5 μl of 20% (w/v) dextran in a PCR tube, resulting in a final reaction volume of 20 μl . The final solution contained 50 mM Tris pH 7.4, 75 mM KCl and 2.5% dextran. This mixture yielded a final protein concentration of 2.5 μM , which is above the saturation concentration (c_{sat}) for condensate formation. As a control condition, protein was added to a final concentration of 0.25 μM (below c_{sat}) under identical buffer conditions. All samples were incubated at room temperature for 60 min to allow for condensate formation. The Ddx4 condensates were prepared using an established protocol^{29,58} by diluting the protein stock 1:1 with a buffer containing 20 mM Tris pH 8. The final Ddx4 concentration in condensate solution was 225 μM and the final Ddx4 concentration in solution without condensates was 45 μM . Samples were incubated at room temperature for 60 min before adding the reactants. The reactions were incubated with the prepared solutions for 1.5 h at room temperature before subjecting the samples for nESI-MS analysis.

Fluorogenic assay for C–N bond formation

4-Amino-1,8-naphthalimide and *N,N*-dimethyl-6-propionyl-2-naphthylamine were used as fluorescent probes for this assay. The probes were first dissolved in a solution composed of 50 wt% methanol and 50 wt% buffer (150 mM NaCl and 50 mM Tris, pH 7.5) to final concentrations of 1.17 mM and 1.11 mM, respectively. The dissolved probes were then mixed into a condensate-containing solution (50 μM protein, 150 mM NaCl and 50 mM Tris, pH 7.5) before characterization using confocal microscopy (Leica Stellaris 8 Falcon). During imaging, the excitation laser was set to 405 nm and emission was collected in three spectral windows: 430–470 nm, 520–540 nm and 555–600 nm. For data analysis, the reaction between 4-amino-1,8-naphthalimide and *N,N*-dimethyl-6-propionyl-2-naphthylamine was monitored by calculating the fluorescence intensity ratio of 555–600 nm to 430–470 nm.

Zeta potential characterization

Zeta potential of condensates was measured at room temperature using a DTS1070 cell, with Henry's function applied at $f(\kappa a) = 1.5$. Condensates for zeta potential measurement were prepared by dialyzing the protein stock solution (4 M urea, 500 mM NaCl and 50 mM Tris, pH 7.5) into a buffer containing 5 mM NaCl and 50 mM Tris (pH 7.5). To minimize the effects of condensate aging during the dialysis process, the formed condensates were briefly heated to 42 °C to be dissolved and then returned to room temperature to reinduce phase separation. SDS and CTAB were added to the solutions containing condensate at a final concentration of 1 mM.

Reporting summary

Further information on research design is available in the Nature Portfolio Reporting Summary linked to this article.

Data availability

All data are available in the main text or Supplementary Information. Additional data supporting the results of this study can be obtained online (<https://osf.io/pf9qn/overview>). The cell metabolomics data are stored on GitHub (https://github.com/xaviersoong/cell_metabolomics_peak_extraction_code_for_condensates_study/tree/main). Source data are provided with this paper.

Code availability

Self-programmed code was written in MATLAB (2025a version) and used for processing cell metabolomics data saved in cdf format. It can be accessed from GitHub (https://github.com/xaviersoong/cell_metabolomics_peak_extraction_code_for_condensates_study/tree/main).

Acknowledgements

R.N.Z. acknowledges support from the Air Force Office of Scientific Research through the Multidisciplinary University Research Initiative program (AFOSR FA9550-21-1-0170) and Stanford Sustainability Accelerator Program (GHG-0030). Y.D. acknowledges the funding support from Alzheimer's Association (AARG-25-1486936) and support from McKelvy School of Engineering and Center for Biomolecular Condensates at Washington University. A.A.H. acknowledges support from the Max Planck Society. R.N.Z. also acknowledges T. McLaughlin at Vincent Coates Foundation Mass Spectrometry Laboratory, SUMS (RRID: SCR_017801) utilizing the Thermo Exploris 240 LC/MS system (RRID: SCR_022216). Part of this work was also performed at nano@stanford (RRID: SCR_026695).

Author contributions

Y.D. and X.S. conceptualized the research. X.S., Y.M., M.W.C. and Y.D. developed the methods. X.S., Y.M., M.W.C., W.Y., X.Y., J.X. and L.L. conducted experimental investigations. X.S., J.X., L.L. and M.W.C. prepared the presentations of the results. R.N.Z. and Y.D. acquired funding support. Y.D., R.N.Z. and A.A.H. administrated the project and

supervised the research. Y.D. and X.S. wrote the original draft. X.S., Y.D., A.A.H. and R.N.Z. reviewed and edited the paper.

Competing interests

The authors declare no competing interests.

Additional information

Supplementary information The online version contains supplementary material available at <https://doi.org/10.1038/s41589-026-02169-2>.

Correspondence and requests for materials should be addressed to Yifan Dai or Richard N. Zare.

Peer review information *Nature Chemical Biology* thanks the anonymous reviewers for their contribution to the peer review of this work.

Reprints and permissions information is available at www.nature.com/reprints.

Reporting Summary

Nature Portfolio wishes to improve the reproducibility of the work that we publish. This form provides structure for consistency and transparency in reporting. For further information on Nature Portfolio policies, see our [Editorial Policies](#) and the [Editorial Policy Checklist](#).

Statistics

For all statistical analyses, confirm that the following items are present in the figure legend, table legend, main text, or Methods section.

n/a Confirmed

- The exact sample size (n) for each experimental group/condition, given as a discrete number and unit of measurement
- A statement on whether measurements were taken from distinct samples or whether the same sample was measured repeatedly
- The statistical test(s) used AND whether they are one- or two-sided
Only common tests should be described solely by name; describe more complex techniques in the Methods section.
- A description of all covariates tested
- A description of any assumptions or corrections, such as tests of normality and adjustment for multiple comparisons
- A full description of the statistical parameters including central tendency (e.g. means) or other basic estimates (e.g. regression coefficient) AND variation (e.g. standard deviation) or associated estimates of uncertainty (e.g. confidence intervals)
- For null hypothesis testing, the test statistic (e.g. F , t , r) with confidence intervals, effect sizes, degrees of freedom and P value noted
Give P values as exact values whenever suitable.
- For Bayesian analysis, information on the choice of priors and Markov chain Monte Carlo settings
- For hierarchical and complex designs, identification of the appropriate level for tests and full reporting of outcomes
- Estimates of effect sizes (e.g. Cohen's d , Pearson's r), indicating how they were calculated

Our web collection on [statistics for biologists](#) contains articles on many of the points above.

Software and code

Policy information about [availability of computer code](#)

Data collection Xcalibur (Thermo Fisher); MATLAB 2025a; Origin 2024; Chemdraw; Graphpad Prism; SIMCA 14.1

Data analysis Xcalibur is used to read mass spectra data and convert data into the cdf format for further processing. Self-coded MATLAB script was used to extract the target metabolite products information from the batch of cdf files. Origin 2024 was used to plot mass spectra; Graphpad prism was used to plot bar graphs and heatmaps; SIMCA was used to do the principal component analysis and draw the score plot. Chemdraw was used to draw chemical structures and reaction diagrams

For manuscripts utilizing custom algorithms or software that are central to the research but not yet described in published literature, software must be made available to editors and reviewers. We strongly encourage code deposition in a community repository (e.g. GitHub). See the Nature Portfolio [guidelines for submitting code & software](#) for further information.

Data

Policy information about [availability of data](#)

All manuscripts must include a [data availability statement](#). This statement should provide the following information, where applicable:

- Accession codes, unique identifiers, or web links for publicly available datasets
- A description of any restrictions on data availability
- For clinical datasets or third party data, please ensure that the statement adheres to our [policy](#)

Accession codes, mass spectra, and relevant data in Figures will be available after publication.

Research involving human participants, their data, or biological material

Policy information about studies with [human participants or human data](#). See also policy information about [sex, gender \(identity/presentation\), and sexual orientation](#) and [race, ethnicity and racism](#).

Reporting on sex and gender	<input type="text" value="not applicable"/>
Reporting on race, ethnicity, or other socially relevant groupings	<input type="text" value="not applicable"/>
Population characteristics	<input type="text" value="not applicable"/>
Recruitment	<input type="text" value="not applicable"/>
Ethics oversight	<input type="text" value="not applicable"/>

Note that full information on the approval of the study protocol must also be provided in the manuscript.

Field-specific reporting

Please select the one below that is the best fit for your research. If you are not sure, read the appropriate sections before making your selection.

Life sciences Behavioural & social sciences Ecological, evolutionary & environmental sciences

For a reference copy of the document with all sections, see [nature.com/documents/nr-reporting-summary-flat.pdf](https://www.nature.com/documents/nr-reporting-summary-flat.pdf)

Life sciences study design

All studies must disclose on these points even when the disclosure is negative.

Sample size	<input type="text" value="No statistical methods were used to predetermine sample size."/>
Data exclusions	<input type="text" value="There is no data that were excluded from the analyses"/>
Replication	<input type="text" value="3 to 5 per group"/>
Randomization	<input type="text" value="All in vitro and in vivo samples were allocated into different groups randomly"/>
Blinding	<input type="text" value="All samples were tested without knowing the grouping identities until disclosure later after data acquisition"/>

Reporting for specific materials, systems and methods

We require information from authors about some types of materials, experimental systems and methods used in many studies. Here, indicate whether each material, system or method listed is relevant to your study. If you are not sure if a list item applies to your research, read the appropriate section before selecting a response.

Materials & experimental systems

n/a	Included in the study
<input checked="" type="checkbox"/>	<input type="checkbox"/> Antibodies
<input type="checkbox"/>	<input checked="" type="checkbox"/> Eukaryotic cell lines
<input checked="" type="checkbox"/>	<input type="checkbox"/> Palaeontology and archaeology
<input checked="" type="checkbox"/>	<input type="checkbox"/> Animals and other organisms
<input checked="" type="checkbox"/>	<input type="checkbox"/> Clinical data
<input checked="" type="checkbox"/>	<input type="checkbox"/> Dual use research of concern
<input checked="" type="checkbox"/>	<input type="checkbox"/> Plants

Methods

n/a	Included in the study
<input checked="" type="checkbox"/>	<input type="checkbox"/> ChIP-seq
<input checked="" type="checkbox"/>	<input type="checkbox"/> Flow cytometry
<input checked="" type="checkbox"/>	<input type="checkbox"/> MRI-based neuroimaging

Eukaryotic cell lines

Policy information about [cell lines and Sex and Gender in Research](#)

Cell line source(s)	<input type="text" value="sf9 cell line is acquired from ThermoFisher scientific."/>
---------------------	--

Authentication	Cell line is authenticated by the vendor.
Mycoplasma contamination	All cell lines are tested negative for mycoplasma contamination.
Commonly misidentified lines (See ICLAC register)	no commonly misidentified lines.

Plants

Seed stocks	N/A
Novel plant genotypes	N/A
Authentication	N/A